GEOCHEMISTRY

# Reexamination of 2.5-Ga "whiff" of oxygen interval points to anoxic ocean before GOE

**Sarah P. Slotznick[1]*, Jena E. Johnson[2], Birger Rasmussen[3,4], Timothy D. Raub[5,6], Samuel M. Webb[7], Jian-Wei Zi[4], Joseph L. Kirschvink[8,9], Woodward W. Fischer[8]**



**Transient appearances of oxygen have been inferred before the Great Oxygenation Event (GOE) [~2.3 billion years (Ga) ago] based on redox-sensitive elements such as Mo and S—most prominently from the ~2.5-Ga Mount McRae Shale in Western Australia. We present new spatially resolved data including synchrotron-based x-ray spectroscopy and secondary ion mass spectrometry to characterize the petrogenesis of the Mount McRae Shale. Sediments were primarily composed of organic matter and volcanic ash (a potential source of Mo), with U-Pb ages revealing extremely low sedimentation rates. Catagenesis created bedding-parallel microfractures, which subsequently acted as fluid pathways for metasomatic alteration and recent oxidative weathering. Our collective observations suggest that the bulk chemical datasets pointing toward a "whiff" of oxygen developed during postdepositional events. Nonzero $\Delta^{33}S$ in trace-metal–poor, early diagenetic pyrite and the unusually enriched organic carbon at low sedimentation rates instead suggest that environmental oxygen levels were negligible ~150 million years before the GOE.**

## INTRODUCTION

All biogeochemical cycling on Earth changed abruptly, fundamentally, and permanently with the rise of atmospheric oxygen at ~2.3 billion years (Ga) ago. Although the Great Oxygenation Event (GOE) has been recognized for over 50 years (*1*, *2*), its drivers are poorly understood. To understand the interlinked biological questions of how oxygenic photosynthesis evolved and when the biosphere first faced molecular oxygen, extensive study has focused on signals for oxygen before the GOE [e.g., (*3*–*6*)].

Atmospheric oxygen levels cannot be measured directly in ancient rocks, forcing the community to rely on indirect proxies. Interpreting redox proxies for ancient marine conditions is extremely difficult, from inherent complexities in depositional patterns [e.g., (*7*)] to known transformations during diagenesis [e.g., (*8*–*10*)] to the introduction of fluids and altering effects of metamorphism and metasomatism [e.g., (*11*, *12*)]. Closely examining the sedimentological context of these redox proxies is critical, as determining the host mineral and textural context of a redox proxy can lead to added confidence or uncertainty in the trustworthiness of geochemical signals [e.g., (*13*–*15*)].

One of the first sedimentary records proposed to document trace levels of local oxygen before the global GOE is the heavily studied ~2.5-Ga Mount McRae Shale (*3*, *16*). In a multifaceted argument developed over the past decade, several different lines of evidence have been brought to bear (*3*, *16*–*24*). For example, Anbar *et al.* (*3*) identified a ~28-m section of shale with high Mo content, correlating roughly with enrichments in total organic carbon (TOC) and Re, which was not seen in the overlying shales or in a lower shale unit (Fig. 1). They interpreted these trace metal enrichments to indicate oxidative weathering of terrestrial sulfides, releasing Mo and Re that was carried by rivers to the ocean and accumulated in oxygenated seawater. Kaufman *et al.* (*16*), on the other hand, pointed to negative $\delta^{34}S$ values and positive $\Delta^{33}S$ in the upper half of the Mount McRae Shale as indicating an increase in atmospheric oxygen and a stratified ocean, although they noted that the Mo-enriched interval contained mostly negative $\delta^{34}S$ and $\Delta^{33}S$ values, and a sharp positive $\Delta^{33}S$ and $\delta^{34}S$ anomaly existed in the lower shale unit. Further work has expanded to other elements and isotopic systems (N, Fe, Mo, U, Os, Se, Th, Hg) but interpreted results in the context of these initial observations of trace metals and sulfur isotopes.

These proxies for oxygen show perturbations focused in the same general area, but if looked at on a detailed stratigraphic sample-by-sample basis, not all indicators are noted. This variability raises the question as to whether these differences are due to aspects of the elemental systems themselves or biogeochemical processing or whether the discordant signals reflect postdepositional processes. To deconvolve its depositional and geologic history, we applied in situ techniques and petrographic observations to fully characterize the sedimentology and geological context of the Mount McRae Shale. In addition to providing deeper contextual understanding, we present a revised sedimentological and petrogenetic framework for this formation that leads to distinctly different interpretations from previous authors and documents a new mode of organic carbon deposition and preservation in pre-GOE marine sediments.

### The Mount McRae Shale and ABDP-9

The Mount McRae Shale of the Hamersley Group is interpreted to have been deposited in a continental back-arc setting along the southern margin of the Archean Pilbara craton (*25*). The 2.63- to 2.45-Ga Hamersley Group preserves a lengthy record of volcanism including the deposition of air-fall tuffs and volcaniclastic debris (*26*, *27*) and rhyolites, which are intercalated with mixed carbonate-siliciclastic sequences and iron formations (*28*). The platform is interpreted to have had an open connection with the ocean during the sediment-starved hemipelagic sedimentation of the Mount McRae

[1]Department of Earth Sciences, Dartmouth College, Hanover, NH 03755, USA. [2]Department of Earth and Environmental Sciences, University of Michigan, Ann Arbor, MI 48103, USA. [3]School of Earth Sciences, The University of Western Australia, Perth, WA 6009, Australia. [4]State Key Laboratory of Geological Processes and Mineral Resources, China University of Geosciences, Wuhan, Hubei 430074, China. [5]School of Earth and Environmental Sciences, University of St Andrews, St Andrews, Fife, KY16 9AL, Scotland, UK. [6]Geoheritage Research Institute, Arlington Heights, IL 60005, USA. [7]Stanford Synchrotron Radiation Lightsource, Stanford University, Menlo Park, CA 94025, USA. [8]Division of Geological and Planetary Sciences, California Institute of Technology, Pasadena, CA 91125, USA. [9]Earth-Life Science Institute, Tokyo Institute of Technology, Tokyo 152-8550, Japan.
*Corresponding author. Email: sslotz@dartmouth.edu

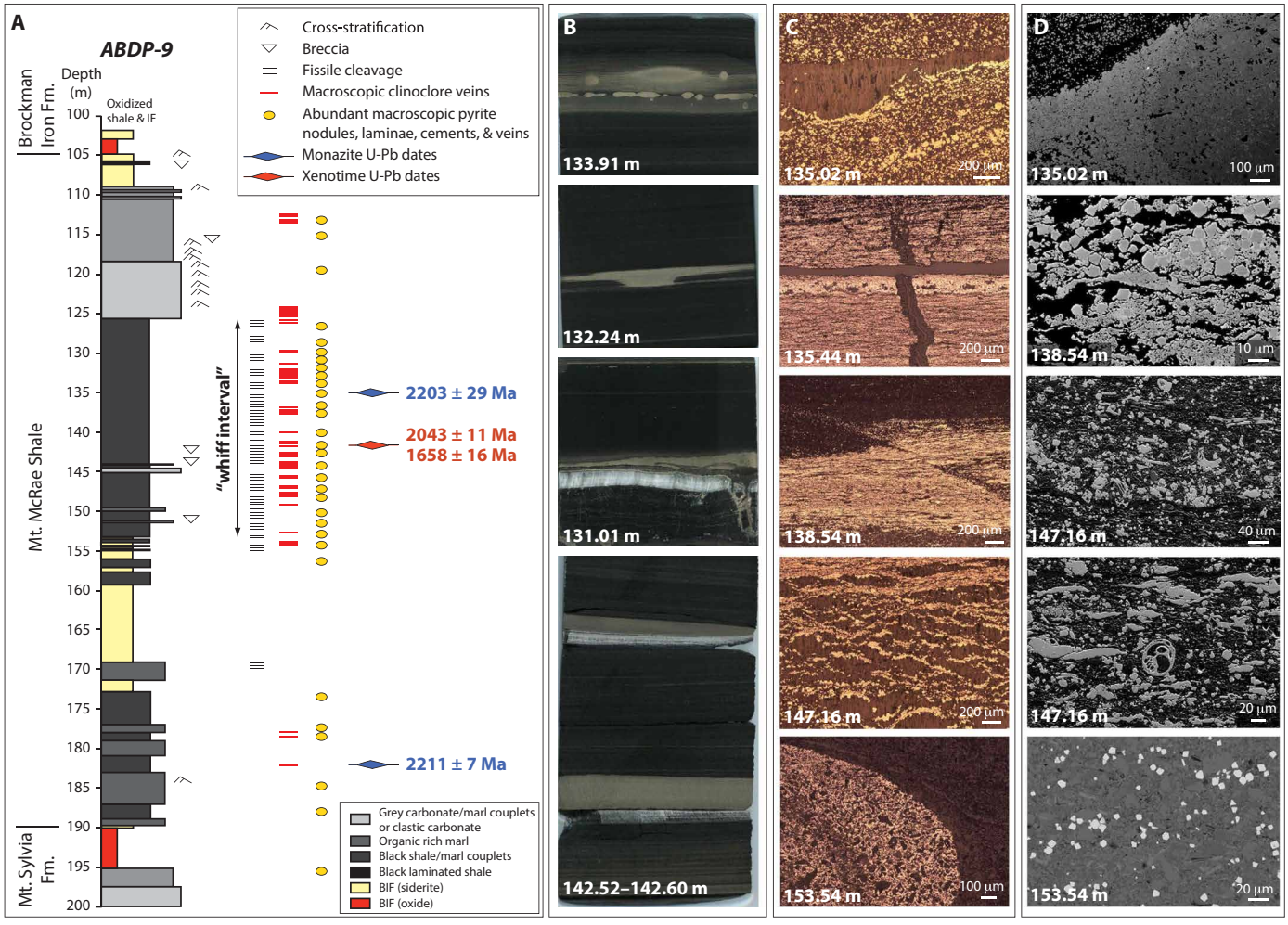


**Fig. 1. Multiscale evidence for postdepositional sulfide mineralization.** (**A**) Stratigraphic column of ABDP-9 focused on Mount McRae Shale from (*3*). Interval where evidence for whiff of oxygen is highlighted by black arrow; this section notably coincides with fissile cleavage (see Fig. 4), clinochlore veins, and extensive pyrite mineralization. Monazite and xenotime, often intergrown with clinochlore veins, dated post-GOE between ~1650 and 2200 Ma. BIF, banded iron formation; Fm., Formation. (**B**) Examples of early pyrite nodules deforming surrounding laminae with secondary pyrite halos (133.91 m) and pyrite in planar laminations closely associated with bedding-parallel clinochlore veins (132.24, 131.01, and 142.52 to 142.60 m). (**C**) Pyrite euhedra and clotted euhedra in sedimentary matrix concentrated against clinochlore seams (135.02 m); seams and clotted pyrite euhedra cross-cut by vertical clinochlore vein (135.44 m); compressional faulting of pyrite-rich seam with additional pyrite euhedra following fault (138.54 m); pyrite seams intergrown with clinochlore-filled overpressure veins with euhedral pyrite overgrowths (147.16 m); early diagenetic pyrite nodule that includes pyritized volcanic clasts (153.54 m). (**D**) Pyrite nodule with brighter (As-rich) overgrowth with an accessory metal sulfide (white) (135.02 m); euhedral pyrite crystals with As-rich pyrite overgrowth and cement (138.54 m); two examples of sulfide-mineralized volcaniclastic particles and glass (147.16 m); euhedral pyrite crystals cross-cutting shale particles (153.54 m).

Shale and overlying Brockman Iron Formation (*25*, *28*). Early diagenetic mineralization has been previously noted in the organic-carbon–rich Mount McRae Shale with pyrite throughout and siderite in the uppermost Colonial Chert Member (*28*). After deposition, the Mount McRae Shale was intruded by mafic sills at 2.45 and 2.22 Ga and subsequently deformed during the 2.20- to 2.15-Ga Ophthalmia orogeny (*29*). Episodic fluid flow events occurred throughout this time period and beyond (dated at 2.40 to 1.66 Ga) (*30*, *31*), perhaps extending back to 2.43 to 2.38 Ga [based on isotopic resetting of zircons in the overlying Brockman Iron Formation; (*26*)].

The ABDP-9 drill core, which was drilled by the NASA Astrobiology Drilling Program in 2004, contains a complete section of the Mount McRae Shale (105.13 to 190.08 m). It has been heavily sampled and analyzed with an array of elemental abundance and isotopic redox tracers focused on trace elements, sulfur, and iron (*3*, *16*–*24*, *32*). Analyses of this carbonaceous black shale are often interpreted to record a "whiff" of oxygen from ~153- to 125-m core depth, a transient appearance of $O_2$ (Fig. 1) (*3*). However, the sedimentation, lithification, postdepositional mineralization, and weathering of the rocks in this interval have not been well characterized. The lack of petrogenetic information has raised questions: How did these rocks form and to what degree do they record environmental redox proxies versus postdepositional alteration?

## RESULTS

We report here new sedimentological observations made on the ABDP-9 drill core with a focus on the Mount McRae Shale including flat-bed optical scanning of the entire core (Fig. 1). On the basis of these observations, 20 samples were collected, spanning from

110- to 370-m core depth, and used to prepare polished thin sections for additional analyses. To characterize the mineralogy and chemistry and to order the relative timing of mineralization using textural relationships, we performed optical and chemical imaging including optical microscopy, electron microscopy with energy-dispersive spectroscopy (EDS), synchrotron-based x-ray fluorescence (XRF), x-ray absorption near-edge spectroscopy (XANES) microprobe imaging, and secondary ion mass spectrometry (SIMS). Additional in situ U-Pb geochronology was conducted on zircon crystals in two tuff beds near the top and base of the Mount McRae Shale, providing constraints on sedimentation rates.

Our observations revealed that the bulk of the Mount McRae Shale was deposited as mud-sized particles settling by suspension with occasional carbonate grainstones associated with mass flows. Widespread parallel lamination developed, at some depths, into fissile cleavage along bedding-parallel and bedding-subparallel fractures (Fig. 1). The new SIMS U-Pb zircon depositional ages of 2533 ± 6 million years (Ma ago) and 2483 ± 7 Ma (figs. S1 to S4) reveal exceptionally low sedimentation rates of 1.03 to 1.76 m/Ma for the Mount McRae Shale, similar to hemipelagic sediment accumulation below mid-ocean gyres (fig. S5).

The sediment is composed of a mixture of volcaniclastic debris and organic carbon detritus cemented with carbonate and chert, later mineralized by abundant pyrite and minor authigenic phases (Fig. 1). More specifically, petrography of the shales revealed that former glass and pyroclastic fragments were preserved or replaced by pyrite (Fig. 1, C and D). We observed macroscopic pyrite, nodules, laminae, cements, and pyrite-filled veins throughout the shale; we analyzed the trace elements and sulfur isotopes preserved in this pyrite using XRF imaging and SIMS point analyses (Figs. 2 and 3 and figs. S8 to S19). These multiple generations of pyrite formation had distinct chemical and isotopic signatures; early diagenetic textures had low Mo and As, more depleted $\delta^{34}S$, and a tight negative $\Delta^{33}S$ clustered around −1‰, which contrasted with later fabrics that had variable but positive $\Delta^{33}S$ often with high Mo and As concentrations.

Late-stage clinochlore veins [identified using x-ray diffraction (XRD); fig. S6] were observed throughout the Mount McRae Shale, often linked stratigraphically to regions with fissile cleavage (Figs. 1 and 4). Previously published monazite and xenotime ages associated with these clinochlore veins confirmed their postdepositional emplacement with multiple ages ranging from ~250 to 850 Ma after deposition (Fig. 1) (*31*). Within these fissile regions, generations of isopachous cements filled the fractures with phyllosilicates and hydrated calcium sulfates in "stringers," with sulfate mineralization likely the most recent event (Fig. 4).

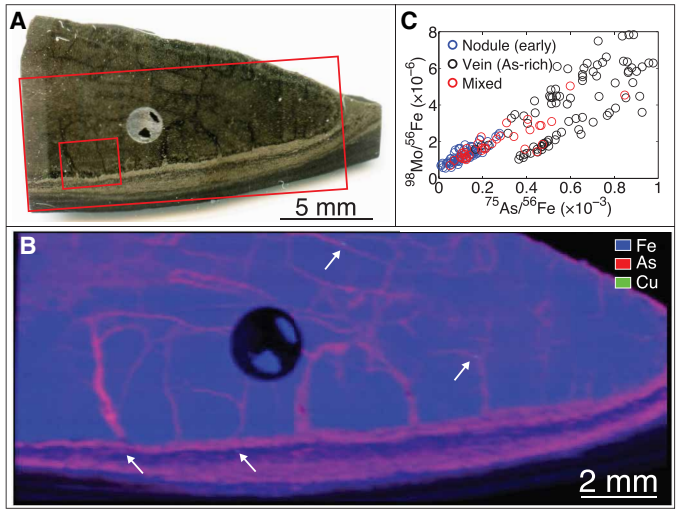


**Fig. 2. Petrographic relationships of metals.** (**A**) Photographic scan of pyrite nodule at 138.09 m highlighting multiple generations of sulfide formation—early nodular formation with later rim and cross-cross pattern of veins. The circle containing irregular chips is an impregnated pyrite standard. The red rectangles show regions focused on in (B) and Fig. 3. (**B**) Synchrotron XRF map of the same thin section, with metals color-coded. Arsenic is found in the features representing postdepositional alteration events (the veins and the rim). White arrows point to a few of the more discrete copper-bearing phases. XRF maps were not standardized, so each element's abundance is relative to highs/lows of the target region. (**C**) Correlation between molybdenum and arsenic using SIMS measurements in pyrite of the same sample. A diversity of molybdenum abundances was found with a strong correlation between high-molybdenum and arsenic-rich sites, which petrographically are shown to be late. The distinct trendlines suggest multiple generations or evolution of fluids.

## DISCUSSION

Our comprehensive sedimentological, petrographic, and chemical observations have placed the Mount McRae Shale in a broader sedimentological context and enabled us to create a paragenetic sequence for the minerals it contains. We interpreted this sequence to understand petrogenesis for the Mount McRae Shale from its deposition to the present, with implications and distinct interpretations for redox proxies measured in previous studies (Fig. 5).

Mount McRae Shale was deposited in a sediment-starved environment with extremely low depositional rates. As pyroclastic debris, much of the sediment settled from suspension with minimal detrital input from rivers, creating a uniquely immature composition for a fine-grained shale. Our observations of abundant pyroclastic glass shards and intercalated tuff beds, paired with the recent insight that volcanic glass is a major host of Mo (*33*), offer a new explanation for the Mo enrichments in the whiff interval. Specifically, Mo from enriched volcanic glass could have been released following dissolution and replacement by sulfides and silicates [e.g., (*34*)] (Fig. 1) and subsequently concentrated in the pyrite and organic-rich, permeable whiff interval. Re enrichments in the ABDP-9 core follow the Mo enrichments (*3*); notably, Re is highly volatile during basaltic eruptions and, like Mo, is relatively enriched in volcanic glass (*35*). This potential source would disconnect Mo (and Re) enrichments from records of marine biogeochemical processes.

Another important component of the whiff interval is the high organic matter, which gradually accumulated because of the low sedimentation rates. Oxygen exposure time is a major control on the amount of preserved organic matter in modern environments (*36*), especially in regions of low sediment accumulation such as the South Pacific gyre (*37*). The Mount McRae Shale contains ~5% TOC reaching 15% TOC in the whiff interval (*3*); this is two orders of magnitude higher than similar sediments from the Cretaceous to present time (fig. S5). This abnormally high level of organic matter preservation suggests that either primary productivity was much higher at ~2.5 Ga compared to the modern ocean or oxygen exposure time is not a major control due to low levels of oxygen and/or the presence of different microbial metabolisms [e.g., (*38*)]. Elevated primary productivity and organic matter deposition would be inconsistent with current understanding of early life and the C cycle

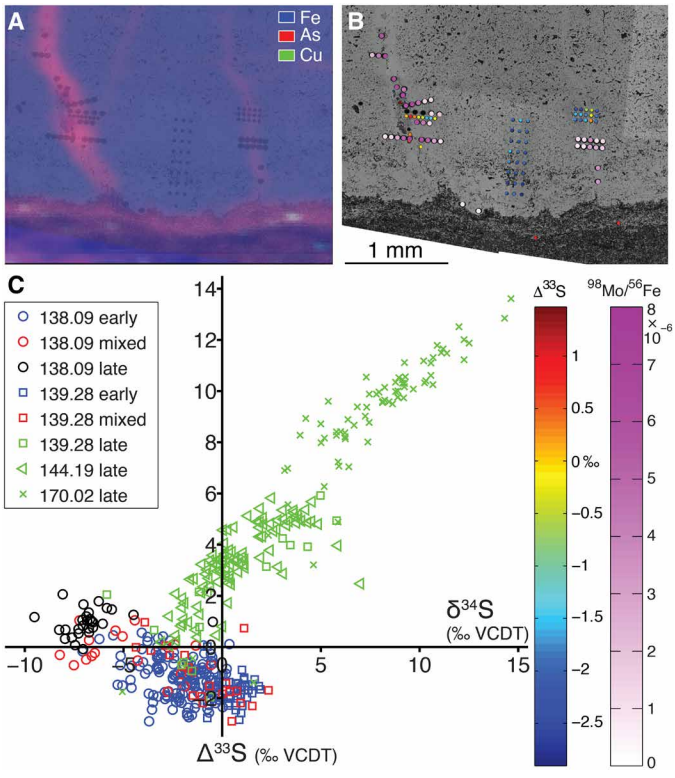


**Fig. 3. SIMS measurements of S isotopes and metals.** (**A**) XRF map on the edge of the pyrite nodule at 138.09 m (Fig. 2) with overlay of reflected light images showing where SIMS measurements were collected. (**B**) $\Delta^{33}$S and Mo abundance are plotted visually on the thin section of 138.09 m. Clear trends are noticeable with higher $\Delta^{33}$S along veins that also have higher molybdenum (and arsenic) concentrations. Analysis of $\Delta^{33}$S fine-grained pyrite outside the nodule also contains higher values and abundant arsenic. (**C**) Combined S isotope measurements from four samples where each measurement was labeled as early, mixed, or late based on petrography (see figs. S13 to S16). Early pyrite textures have slightly negative $\Delta^{33}$S and near-zero to slightly negative $\delta^{34}$S, whereas late textures show an increase in $\Delta^{33}$ and disparate changes in $\delta^{34}$S. Similar trends are noted between samples suggesting that patterns are not related to stratigraphy, but instead due to multiple generations of fluids moving through these samples, recrystallizing pyrite and affecting metal and S isotopic compositions. VCDT, Vienna Canyon Diablo Troilite.

(*39*–*41*), prompting us to favor the latter interpretation that organic carbon was exposed to little or no oxygen during its accumulation and early diagenesis.

Petrographic observations and chemical imaging showed widespread pyrite mineralization throughout the whiff interval ranging from early diagenetic nodule growth to late cross-cutting mineralization (Fig. 1). The best evidence for syndepositional pyrite mineralization comes from early pyrite nodules deforming surrounding laminae with differential compaction, suggesting growth before lithification (Fig. 1B, top). Delicate pyroclastic glass fabrics were remineralized as pyrite or preserved within large pyrite nodules in this early diagenetic process (Fig. 1, C and D). This early mineralization was localized, suggesting limitations in either sulfate, sulfide, or reactive iron [e.g., (*18*)] and the presence of chemically distinct microenvironments. Although wide ranges in sulfur isotopes were noted across the multiple pyrite generations, early diagenetic pyrite had a depleted $\delta^{34}$S signature (mean = −1.41‰, range = −6.22 to 1.94‰) and negative $\Delta^{33}$S (mean = −1.33‰, range = −2.90 to 0.56‰) (Fig. 3), consistent with the findings of a previous SIMS-based study (*32*). These values are similar to rocks from South Africa of a similar age with comparable large pyrite nodules (*42*), although greater differences were noticed within and between early nodules in that study. We interpret these S isotopes in early pyrite to record the role of microbial sulfate reduction during early diagenesis and indicate less than $10^{-6}$ atm atmospheric oxygen levels due to the presence of nonzero $\Delta^{33}$S (*43*).

The formation of secondary bedding-parallel fractures within this organic-rich sediment facilitated the fluid flow required for later pyrite and other hydrothermal mineralization (Fig. 1). Similar microfractures are abundant in petroleum source rocks due to the development of fluid overpressure during thermal maturation and formation of oil and gas [e.g., (*44*–*47*)]. Extrapolated metamorphic index minerals from underlying mafic rocks of the Fortescue Group suggest that the Mount McRae Shale in the region of drill-hole ABDP-9 is in the prehnite-pumpellyite-epidote zone (Zone II), resulting in estimated temperatures of 200° to 300°C assuming only burial metamorphism (*48*, *49*); these temperatures exceed those required for oil and gas generation [~95° to 155°C; (*50*)]. Previous microscale analytical study of pyrobitumen and kerogen in ABDP-9 suggested petroleum generation and/or migration (*32*). Thus, we interpret that the bedding-parallel and bedding-subparallel fractures in the organic-rich intervals of the Mount McRae Shale (Fig. 1) originally formed during maturation and fluid overpressure associated with petroleum expulsion (Fig. 5). These fractures developed into fissile cleavage that is most pronounced in the whiff interval because of its higher TOC (Fig. 1).

Hydrothermal fluids used these fractures as conduits and precipitated later diagenetic phases including clinochlore and other phyllosilicates (Fig. 5). Clinochlore, a chlorite mineral, is often found in macroscopic bedding-parallel veins concentrated within the whiff interval (Fig. 1, A and B). Fluid overpressure during these events led to the formation of additional horizontal and later vertical fractures (Figs. 1 and 5). Chlorite thermometry on these minerals indicated that they precipitated from hot fluids at temperatures varying from 230° to 320°C (error ± 50°C) (*31*, *51*). In situ U-Pb geochronology of monazite and xenotime in bedding-parallel overpressure veins associated with clinochlore reveals metasomatic events at ~2.20, ~2.05, and ~1.66 Ga in the whiff interval (*31*).

In addition to these clinochlore veins, we observed extensive secondary (epigenetic) iron sulfide mineralization. Pyrite formed as rims around previously existing nodules, in veins within nodules and associated with clinochlore in laminae and seams, as cross-cutting euhedral crystals in the matrix, and in rims around these euhedral crystals (Figs. 1, 2, and 4 and figs. S7 and S13 to S16). Secondary blocky pyrite crystals with petrographically distinct and brighter (higher average atomic number) rims suggest at least two remineralization events. This texturally late pyrite was enriched in heavy metals such as Mo and As, which we interpret derived from hydrothermal mineralization [Fig. 2 and figs. S7 to S9 and S11; e.g., (*52*)]. Pyrite textures and fabrics identified as postdepositional contained, on average, five times more Mo than early textures (based on SIMS data; Fig. 2C and dataset S1); back-of-envelope calculations using pyrite abundance [up to 20 weight % and, on average, two times more abundant in the whiff interval (*3*, *18*)] show that Mo in secondary pyrite could easily explain the 5-fold (on average) and even the maximum 50-fold enrichment of Mo seen in the whiff interval. The origin of Mo could be either Mo-rich volcanic glasses, externally

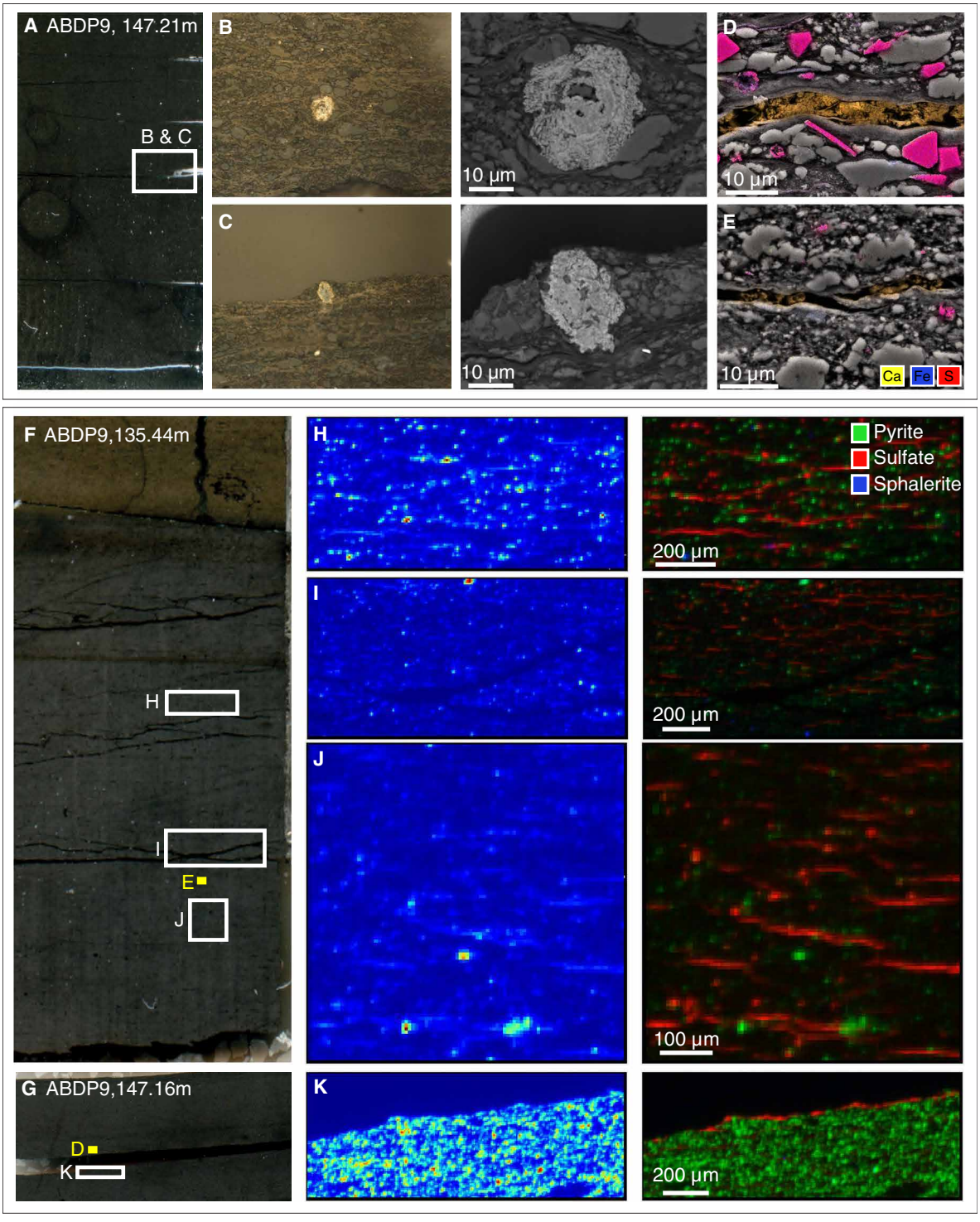


**Fig. 4. Sulfur mineralogy and fissile cleavage within the Mount McRae Shale.** (**A** to **C**) Core scan of 147.21 m containing pyrite nodules (labeled white box), which show evidence for oxidation through dissolution/porous texture and mineral transformations in reflected light and backscatter electron (BSE) images. (**D** and **E**) BSE images overlain by elemental color maps via EDS reveals Ca, S precipitates in bedding-parallel fractures lined by precipitated silicate cements. Ablation due to electron beam (visible pits) suggests that these sulfur phases are hydrated. (**F** and **G**) Core scans displaying fissile nature of the rocks, with labeled locations of BSE images in yellow and XRF maps at multiple S energies in white. (**H** to **K**) XRF maps of total sulfur concentrations at 2490 eV (left column) display sulfur phases distributed throughout the sample. Endmember fitting of XRF maps at multiple S energies (2469.5, 2471, 2472.5, 2476, 2482.5, and 2490 eV) identifies these sulfur minerals (fig. S19), and a mineralogical map can be made (right column). Pyrite and sphalerite are present in distinct "hot spots" as disseminated crystals. However, sulfate occurs in widespread bedding-(sub) parallel fractures as discontinuous stringers and along fracture surfaces, consistent with BSE-EDS observations.

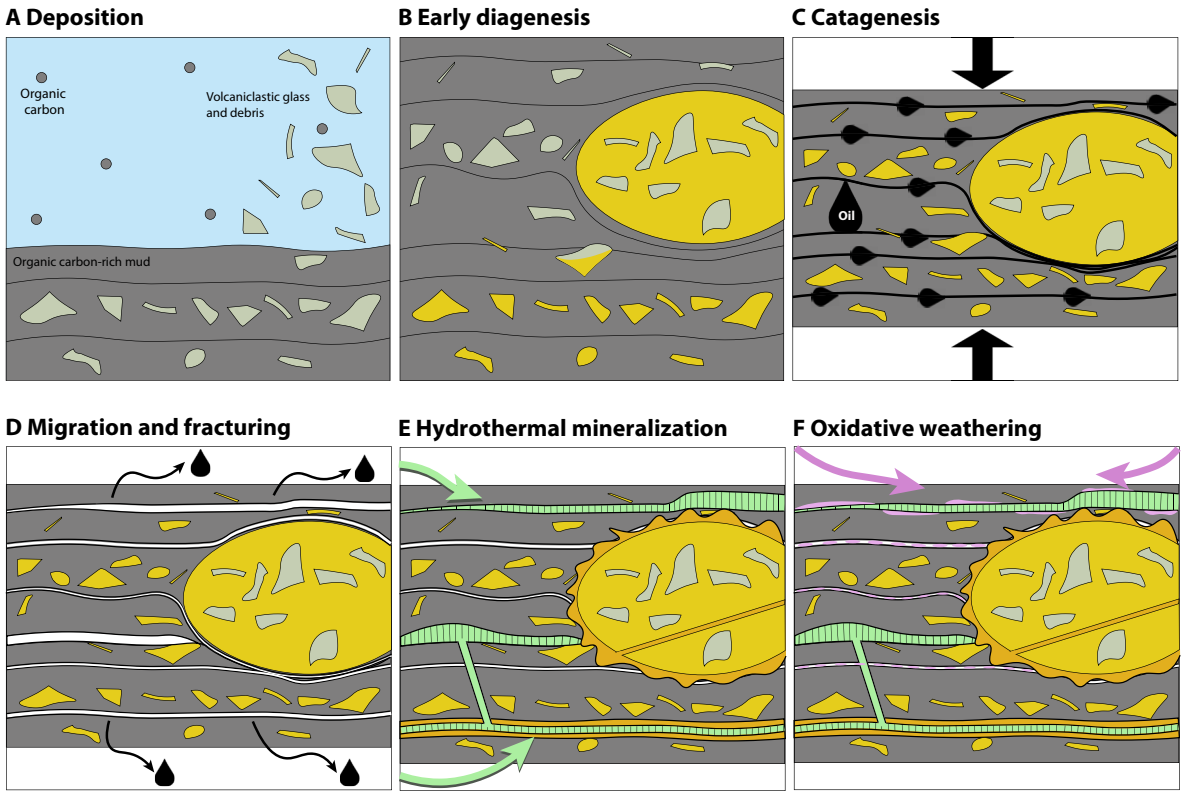


**Fig. 5. Schematic diagram of petrogenesis of Mount McRae Shale based on our observations and geochemical data.** (**A**) Deposition of organic carbon and air-fall volcaniclastic debris. (**B**) Early stages of diagenesis including pyrite nodule growth and pyrite permineralization of sediments. (**C**) Compaction during burial and thermal maturation of organic-rich sediments in catagenesis. (**D**) Hydrocarbon formation leads to episodic fluid overpressure, microfracturing, and hydrocarbon expulsion along bedding-parallel microfractures eventually developing into fissile cleavage. (**E**) Migration of cratonic fluids along microfractures accompanied by at least three episodes of metasomatic mineralization, including pyrite rich in both As and Mo. (**F**) Introduction of meteoric fluids and oxidative weathering resulting in pyrite oxidation and calcium sulfate precipitation along fissile cleavage.

sourced hydrothermal fluids, or Archean ocean water, but at this point, it is impossible to distinguish between them. Prior work on ABDP-9 has shown that Mo isotopes are variable and heavy compared to bulk silicate earth with the heaviest values in the whiff interval, which were interpreted to be due to environmental oxygenation (*19*, *23*). Work in the past decade has shown empirically that hydrothermal mineralization even in magmatic systems yields heavy $\delta^{98}$Mo in pyrite, +1.80 and +2.09‰ (*53*, *54*), akin to what is seen in ABDP-9. We observed a range of $\delta^{34}$S and $\Delta^{33}$S signatures trending toward highly positive values in late-textured pyrite (Fig. 3), which could suggest that later fluids had higher sulfate concentrations (*55*). Late textures in South Africa also contained more positive $\delta^{34}$S and/or more positive $\Delta^{33}$S compared to early pyrite textures (*42*, *56*). Distinct geochemical trends in primary versus secondary textures again demonstrate that multiple generations of fluid flow affected the chemical signature of these rocks. Direct linkage of pyrite mineralization to the dated hydrothermal events is difficult; however, secondary pyrite found in overpressure veins dated at 2.20 and 1.66 Ga links hydrothermal fluids to sulfide precipitation at least locally (*31*). Pyrite-mineralized thrust faults (Fig. 1) suggest that a source for these fluids was basin-wide percolating crustal fluids [e.g., (*57*)] from orogenic events over Proterozoic time.

It has been argued that the trace elements such as Mo in this core have not been affected by postdepositional processes based on the Re-Os isochron (*3*, *22*). Original efforts integrated the depths 128.71 to 129.85 m and 145.22 to 148.32 m and arrived at plausible depositional age based on existing (and our new) U-Pb measurements. However, the initial Re-Os isochron reported in (*3*) yielded a subchrondritic initial $^{187}$Os/$^{188}$Os value (*22*). Follow-up study (*3*, *22*) sought to improve and understand the isochron; eight additional samples were taken from 148.09- to 148.15-m depth. These had initial values that were suprachrondritic and, when combined with the previous lower dataset, yielded a Re-Os age of 2495 ± 14 Ma. [Interpretations of suprachondritic $^{187}$Os/$^{188}$Os values as a proxy for continental oxidative weathering have been called into question due to a lack of Mesoproterozoic-Phanerozoic examples and potential mobilization by hydrothermal fluids (*58*).] Because the Re-Os system yielded an isochron consistent with other ages for these units, it was argued that all the other trace element systems were not disturbed. However, it is important to note that Re-Os and Mo are carried by different mineral phases in black shales. Re-Os are held predominantly by organic matter and secondarily detrital/extraterrestrial silicates (*59*). In contrast, Mo is primarily hosted in sulfide-bearing minerals specifically pyrite, chalcopyrite, and molybdenite (*11*, *34*, *54*). Our analyses in the Mount McRae Shale highlight that Mo is primarily hosted in late As-rich pyrite phases, not in background matrix phases including organic matter (Fig. 2 and figs. S9 and S11). On the other hand, Re and Os have been shown to be hosted in organic phases and remain in organic phases through the process of catagenesis even in overmature sedimentary systems (*60*). Therefore, preservation of

a plausibly depositional Re-Os isochrons need not inform the timing of enrichments of other trace metals.

Most recently, these strata were subjected to oxidizing fluids initiating incipient weathering (Fig. 5). The upper 100 m of ABDP-9 shows visible evidence of oxidative weathering (Fig. 1), consistent with the deep regolith formation in this region of Australia due to the lack of glaciation over the past 290 Ma (*61*). Remarkably, we observed signs of oxidation and weathering extending at least 100 m further through the Mount McRae Shale and into the underlying iron formations (Fig. 4 and figs. S17 and S18). Sulfate stringers were observed in fissile cleavage planes (Fig. 4); these oxidized phases were only identified in regions of fissile cleavages, suggesting a close connection between these fractures, fluid flow, and oxidation (fig. S18). Mudstone beds without fissile textures do not display sulfate mineralization (fig. S18). These cross-cutting hydrated calcium sulfates (e.g., gypsum) were the most recently emplaced phase due to their petrographic relationships with clinochlore and phyllosilicates cements and their incompatibility with the known metamorphic history of these rocks. We interpret these sulfate salts as the product of oxidative weathering as groundwater flowed through these regions. Along the microfractures, meteoric water oxidized pyrite (Fig. 4) and other ferrous iron-bearing minerals, and then, buffered by carbonate dissolution, oxidized species such as sulfate salts and iron oxides precipitated (Fig. 4 and figs. S17 and S18) [e.g., (*62*, *63*)]. Notable, this oxic alteration was concentrated in the whiff interval where the rock was the most fractured due to originally higher concentrations of TOC and petroleum expulsion (Fig. 4).

### Implications

Like all sedimentary rocks, the Mount McRae Shale has a long and complex history of mineralization, hindering an accurate interpretation of paleoredox proxies. Despite being incredibly well preserved for its age, detailed microtextural analyses revealed that the shale has undergone hydrocarbon generation with associated fluid overpressure and microfracturing, facilitating multiple mineralization events of sulfides, silicates, and sulfate salts. In addition, the known enrichment of Mo in volcanic glass, which is abundant in the Mount McRae Shale, offers an alternative pathway for the concentration of Mo in the "whiff of oxygen" interval. This new interpretation of the Mo enrichments would also be consistent with prior investigations of the pre-GOE Mo cycle that concluded a lack of continental oxidative weathering before ~2.4 Ga (*64*, *65*).

Our analyses prompt questions as to which, if any, bulk chemical signals within the strata can be definitively linked to marine conditions at 2500 Ma. It is clear, however, that the Mount McRae Shale had very low sedimentation rates with the major siliciclastic component derived from volcaniclastics, resulting in high organic carbon accumulation. This is a mode of organic carbon cycling and burial that contrasts sharply with observations after the GOE, where the lowest sedimentation rates yield low TOC due to oxygen exposure time. Thus, preservation of these high concentrations of organic matter, as well as early diagenetic pyrite precipitation, indicates protracted anoxic conditions (at least 50 Ma; fig. S5) near the seabed and in pore waters. These observations suggest that environmental oxygen levels were incredibly low ~150 Ma before the GOE, consistent with other redox proxies such as redox-sensitive detrital grains and multiple sulfur isotope fractionation reported during this time [e.g., (*66*–*68*), with the latter proxy captured in early pyrite phases of the Mount McRae Shale].

Our understanding of the rise of oxygen has evolved in the past decade as more studies interpret signals of oxygen before the GOE [e.g., (*4*, *5*)] and raise questions about the nature of the GOE itself. Recent work highlights discordant interpretations between stratigraphic sections and individual redox proxies on the timing of the GOE, whether it was multiple, single, or stepped events, and its relation to climatic events [e.g., (*69*–*72*)]. Different proxies probe different phases, have a range of sensitivities, and view distinct biogeochemical cycles affected by oxygen. They can also be affected by postdepositional processes in different ways, and these processes can vary between and within sections. When proxies disagree, distinguishing between these two alternatives (and the potential for both) is vital. The specific detailed results within this paper showing how postdepositional alteration affected trace metal and S redox proxies necessarily only apply to the Mount McRae Shale. However, the difficulty in interpreting depositional conditions within these rocks is a shared challenge in all ancient rocks. By using a combination of petrographic and texture-based chemical imaging techniques, the accuracy of interpretations made by paleoredox proxies can be tested, evaluated, and refined. The stakes are high as we, as a community, probe ancient redox conditions at critical time points in Earth's history. Because interpretations based on paleo-$O_2$ proxies can be uncertain, multiple working hypotheses about the timing of oxygen's appearance on Earth are warranted.

## MATERIALS AND METHODS

Twenty samples were collected from the ABDP-9 core, which was drilled as part of the Deep Time Drilling Project of the Astrobiology Drilling Program in 2004. The drill site was at 21°59′29.5″S, 117°25′13.6″E in Western Australia. These samples span the stratigraphy from 110- to 370-m core depths with a focus on the Mount McRae Shale from 105 to 190 m and are predominantly black shales with one banded iron formation sample.

### Microtextural methods

Polished thin sections were subsequently made of all samples and studied using reflected and transmitted optical microscopy. Further petrographic observations were made in the Caltech GPS Division Analytical Facility using a Zeiss 1550VP Field Emission scanning electron microscope with a Robinson-type backscatter electron detector for imaging. A paired Oxford X-Max SDD EDS was used to determine x-ray spectra at submicrometer pixels to produce semiquantitative maps of elemental abundance.

#### *Sulfur and iron redox-specific mineralogy*

Although EDS can show elemental abundance, it cannot provide information on the chemical form of elements (oxidation state, orbital electronics, type, and number of neighbors). Therefore, to determine exact speciation and redox states of sulfur and iron-bearing minerals, we used synchrotron-based x-ray microprobe techniques. XANES was paired with XRF imaging using beamlines 2-3 and 14-3 at the Stanford Synchrotron Radiation Lightsource. XANES was performed in fluorescence mode at specific 4- to 16-$\mu m^2$ spots (beam size) on eight thin sections, and differences in the K-edge spectra easily allowed determination of Fe and S redox state and coordination [e.g., (*73*, *74*)]. XRF maps of 4- to 121-$\mu m^2$ pixels were collected at multiple excitation energies over the XANES spectrum: for 2-3: 7120, 7128, 7130, and 7135 eV; for 14-3: 2469.5, 2471, 2472, 2476, 2482.5, and 2490 eV. Images differentiating between phases and redox

state were created by fitting the endmember spectra of different phases from the sample to the XRF maps [e.g., (*75*)]. The incident x-ray energy was set using a Si (111) double-crystal monochromator. At beamline 14-3, the monochromator energy was calibrated by setting the first thiol peak of a sodium thiosulfate powder to 2472.02 eV. At beamline 2-3, the monochromator energy was calibrated by setting the inflection point of a metallic Fe foil to 7112 eV. XRF multiple energy maps were processed using the MicroAnalysis Toolkit (*76*), and XANES data were processed using SIXPack (*77*).

***Trace element presence and abundance***

Synchrotron-based high-energy XRF imaging was performed using beamline 10-2 at the Stanford Synchrotron Radiation Lightsource to characterize elemental abundances of trace metals in 13 thin sections. Incident x-ray energies were applied at 20,200 eV with collecting times of 800 ms to target high-energy K edges of trace elements such as Mo. Elemental abundance maps were produced with 30 × 30 μm pixels using a beam size of ~100 $\mu m^2$. Standards of known concentration for elements of interest were run at the beam time session with the same collection parameters. XRF elemental maps were processed using the MicroAnalysis Toolkit (*76*). Mapping of Mo using a standard energy window was inaccurate due to the overlapping energies of Mo Kα and Zr Kβ, which was present in zircons and in the thin section glass. Therefore, in samples where Mo was indicated, an average XRF spectrum was found by integrating spectra of individual pixels over texturally similar regions to distinguish Mo from Zr. This technique confirmed the presence of Mo in pyrite nodules and the absence of it in the nearby shale matrix in three thin sections (fig. S9).

Mo, Cu, As, (Co, Au, Ni), and Fe concentrations within pyrite were analyzed in situ for three samples using SIMS. Ni was only measured on ABDP9-148.68, and Co and Au were not measured on this sample. The Cameca 7f-GEO, housed at Caltech's Center for Microanalysis, is a pseudo-multicollector SIMS instrument with three separate collectors that measure different ions in rapid succession by dynamic peak hopping. For samples ABDP9-138.09 and ABDP9-144.19, a −12.5-keV $^{16}O^-$ primary beam (21.5-keV impact energy) was used to presputter a ~400-$\mu m^2$ surface with a ~5- to 15-nA current before being applied to a spot size of 25 $\mu m^2$ for acquisition. In each of 20 cycles, we measured $^{56}Fe$ for 0.96 s, $^{59}Co$ for 0.96 s, $^{63}Cu$ for 0.96 s, $^{75}As$ for 0.96 s, $^{95}Mo$ for 4.96 s, $^{97}Mo$ for 4.96 s, $^{98}Mo$ for 4.00 s, and $^{197}Au$ for 2.96 s; typical counts per second (cps) were highest for $^{56}Fe$ at ~106 cps and lowest for Mo isotopes at 1 to 2500 cps. For sample ABDP9-148.68, a −12.5-keV $^{16}O^-$ primary beam (21.5-keV impact energy) was used to presputter a ~100-$\mu m^2$ surface with a ~15-nA current before being applied to a spot size of 100 $\mu m^2$ for acquisition. In each of 10 cycles, we measured $^{56}Fe$ for 0.96 s, $^{60}Ni$ for 4.00 s, $^{63}Cu$ for 2.96 s, $^{75}As$ for 10 s, $^{95}Mo$ for 14.96 s, $^{97}Mo$ for 14.96 s, and $^{98}Mo$ for 14.96 s; typical cps were highest for $^{56}Fe$ at ~106 cps and lowest for Mo isotopes at 0.5 to 100 cps. Ratios were computed for $^{95}Mo/^{98}Mo$ and $^{97}Mo/^{98}Mo$ to check for mass dependence (fig. S10); samples that did not show mass dependence were not included in further analyses. All data are presented as ratios of $^{56}Fe$ to account for yield differences between different measurements (Fig. 2, fig. S11, and dataset S1).

***In situ sulfur isotopes***

Pyrite $\delta^{34}S$ and $\Delta^{33}S$ were measured in situ on four thin section samples at the Caltech's Center for Microanalysis using the Cameca 7f-GEO. A 10-keV $^{133}Cs^+$ primary beam (19-keV impact energy) was used to presputter a ~100-$\mu m^2$ surface with a ~3-nA current before being applied to a spot size of 25 $\mu m^2$ for 10 cycles of acquisition. In each cycle, we measured $^{32}S$ for 0.96 s, $^{33}S$ for 2.96 s, and $^{34}S$ for 2 s; typical counts were ~108 cps for $^{32}S$, ~106 cps for $^{33}S$, and ~107 cps for $^{34}S$. Mass resolving power was between 3000 and 4500 to ensure differentiation of $^{34}S$ intensities from $^{33}SH$. Sample measurements were bracketed in blocks of $10^{-15}$ measurements with four measurements of an in-house pyrite standard ($\delta^{34}S$ 1.024‰ and $\delta^{33}S$ 0.608‰), mounted in epoxy on the sample before it was made into a thin section to obtain a flat analytical surface. Data were corrected for Faraday cup yield differences and instrumental mass fractionation of isotopes (*56*) and are reported in delta notation in per million with respect to Vienna Canyon Diablo Troilite (VCDT) (Fig. 3, fig. S12, and dataset S1).

**X-ray diffraction**

Vein mineral identifications were confirmed using XRD. XRD analyses were made on homogenized sample powder using a two-piece sample powder holder and a PANalytical X'Pert Pro X-ray diffractometer at the California Institute of Technology equipped with a Cu Kα source. Mineralogical identities were confirmed via the resulting spectra using Jade (Materials Data Inc.)

**U-Pb zircon geochronology**

Zircon crystals identified in microtuff layers in polished thin sections from drill holes WLT10 (drill depth, 382.15 m) and ABDP-9 (drill depth, 175.54 to 175.70 m) were analyzed by a sensitive high-resolution ion microprobe (SHRIMP) using established procedures (*78*). Zircon U-Pb dataset was acquired over two analytical sessions using the BR266 zircon standard [$^{206}Pb/^{238}U$ age of 559 Ma, U concentration of 903 parts per million (ppm), z6266 of Stern and Amelin (*79*)] as the primary reference material for calibrating U concentration and U/Pb ratios. Zircon from OG1 [$^{207}Pb/^{206}Pb$ age of 3465 Ma; (*80*)] was used as a secondary standard to monitor the instrumental mass fractionation in $^{207}Pb/^{206}Pb$. Data were reduced using SQUID2 [v2.50; (*81*)] and were calculated and visualized using ISOPLOT3 [v3.75; (*82*)]. Weighted mean ages are quoted at the 95% confidence interval, and individual analyses are presented with 1σ errors. SHRIMP zircon U-Pb data are presented in tables S1 and S2.

***Analytical results, sample WLT10, 382.15 m***

A total of 15 spot analyses were obtained from 14 zircon grains (table S1) from three microtuff layers (fig. S1). The zircons contain moderate to high U and Th concentrations of 331 to 1390 ppm and 167 to 1247 ppm, respectively, with high Th/U ratios varying from 0.45 to 1.73 (mean, 0.79), consistent with magmatic origin. All analyses have low common Pb fractions ($f_{206}$ < 0.4%), although five record large discordance (≥17%) (fig. S2). The five most discordant analyses are from zircon grains with the highest U and Th contents, suggesting that the discordance may be ascribed to Pb loss induced by radiation damage of the crystals. The best dataset comprises seven concordant (i.e., within 5% discordance) and two near-concordant (5 to 10% discordance) data points, all of which have moderate U and Th contents. Combining the nine best data points yields a weighted mean $^{207}Pb/^{206}Pb$ date of 2483 ± 7 Ma [mean square of weighted deviates (MSWD) = 1.16, $n$ = 9], which is considered as the best estimation of the depositional age of the tuffs. One zircon grain yielded a significantly younger concordant $^{207}Pb/^{206}Pb$ date and is treated as a statistical outlier. Although from a distinct core, this sample was correlated to ABDP-9 at 110.5 m due to its collection 3 m

below the base of the Colonial Chert, an informal distinctive member at the top of the Mount McRae Shale.

***Analytical results, sample ABDP-9, 175.54 to 175.70 m***

Twenty-nine spot analyses were conducted on 14 zircon grains (table S2) from a 1-mm-thick tuff layer (fig. S3). The zircon grains have moderate to high U concentrations in the range of 220 to 1089 ppm (mean, 410 ppm) and elevated Th/U ratios varying from 0.55 to 8.54 (mean, 1.58). Although all 29 analyses record low common $^{206}Pb$ ($f_{206}$ < 1%), 14 of them are >10% discordant, indicating variable degrees of Pb loss. The best dataset includes eight concordant and six near-concordant analyses, which give a weighted mean $^{207}Pb/^{206}Pb$ date of 2533 ± 6 Ma (MSWD = 0.45, $n$ = 14). One analysis yielded a younger $^{207}Pb/^{206}Pb$ date of 2499 ± 6 Ma (1σ) and was disregarded in determination of weighted mean date. All analyses define a discordia line that intercepts the concordia curve at 2541 ± 15 Ma (fig. S4). The weighted mean $^{207}Pb/^{206}Pb$ age of 2533 ± 6 Ma is considered the best approximation of the age of the zircons and the depositional age of the tuff.

## SUPPLEMENTARY MATERIALS

Supplementary material for this article is available at https://science.org/doi/10.1126/sciadv.abj7190

## REFERENCES AND NOTES


1. L. Berkner, L. Marshall, *The History of Growth of Oxygen in the Earth's Atmosphere* (John Wiley & Sons Inc., 1964).
2. P. E. Cloud Jr., Atmospheric and hydrospheric evolution on the primitive earth. *Science* **160**, 729–736 (1968).
3. A. D. Anbar, Y. Duan, T. W. Lyons, G. L. Arnold, B. Kendall, R. A. Creaser, A. J. Kaufman, G. W. Gordon, C. Scott, J. Garvin, R. Buick, A whiff of oxygen before the Great Oxidation Event? *Science* **317**, 1903–1906 (2007).
4. A. D. Czaja, C. M. Johnson, E. E. Roden, B. L. Beard, A. R. Voegelin, T. F. Nagler, N. J. Beukes, M. Wille, Evidence for free oxygen in the Neoarchean ocean based on coupled iron-molybdenum isotope fractionation. *Geochim. Cosmochim. Acta* **86**, 118–137 (2012).
5. S. A. Crowe, L. N. Døssing, N. J. Beukes, M. Bau, S. J. Kruger, R. Frei, D. E. Canfield, Atmospheric oxygenation three billion years ago. *Nature* **501**, 535–538 (2013).
6. H. Ohmoto, A seawater-sulfate origin for early Earth's volcanic sulfur. *Nat. Geosci.* **13**, 576–583 (2020).
7. G. R. Helz, E. Bura-Nakic, N. Mikac, I. Ciglenecki, New model for molybdenum behavior in euxinic waters. *Chem. Geol.* **284**, 323–332 (2011).
8. C. M. Hansel, C. J. Lentini, Y. Tang, D. T. Johnston, S. D. Wankel, P. M. Jardine, Dominance of sulfur-fueled iron oxide reduction in low-sulfate freshwater sediments. *ISME J.* **9**, 2400–2412 (2015).
9. J. L. Morford, W. R. Martin, C. M. Carney, Rhenium geochemical cycling: Insights from continental margins. *Chem. Geol.* **324-325**, 73–86 (2012).
10. Y. Wang, I. L. Hendy, J. C. Latimer, D. Bilardello, Diagenesis and iron paleo-redox proxies: New perspectives from magnetic and iron speciation analyses in the Santa Barbara Basin. *Chem. Geol.* **519**, 95–109 (2019).
11. O. H. Ardakani, A. Chappaz, H. Sanei, B. Mayer, Effect of thermal maturity on remobilization of molybdenum in black shales. *Earth Planet. Sci. Lett.* **449**, 311–320 (2016).
12. S. P. Slotznick, J. Eiler, W. W. Fischer, The effects of metamorphism on iron mineralogy and the iron speciation redox proxy. *Geochim. Cosmochim. Acta* **224**, 96–115 (2018).
13. M. Gomes, D. Fike, K. Bergmann, C. Jones, A. Knoll, Environmental insights from high-resolution (SIMS) sulfur isotope analyses of sulfides in proterozoic microbialites with diverse mat textures. *Geobiology* **16**, 17–34 (2018).
14. C. Mahoney, C. März, J. Buckman, T. Wagner, V.-O. Blanco-Velandia, Pyrite oxidation in shales: Implications for palaeo-redox proxies based on geochemical and SEM-EDX evidence. *Sediment. Geol.* **389**, 186–199 (2019).
15. N. J. Planavsky, L. J. Robbins, B. S. Kamber, R. Schoenberg, Weathering, alteration and reconstructing Earth's oxygenation. *Interf. Focus* **10**, 20190140 (2020).
16. A. J. Kaufman, D. T. Johnston, J. Farquhar, A. L. Masterson, T. W. Lyons, S. Bates, A. D. Anbar, G. L. Arnold, J. Garvin, R. Buick, Late Archean biospheric oxygenation and atmospheric evolution. *Science* **317**, 1900–1903 (2007).
17. J. Garvin, R. Buick, A. D. Anbar, G. L. Arnold, A. J. Kaufman, Isotopic evidence for an aerobic nitrogen cycle in the latest archean. *Science* **323**, 1045–1048 (2009).
18. C. T. Reinhard, R. Raiswell, C. Scott, A. D. Anbar, T. W. Lyons, A late Archean sulfidic sea stimulated by early oxidative weathering of the continents. *Science* **326**, 713–716 (2009).
19. Y. Duan, A. D. Anbar, G. L. Arnold, T. W. Lyons, G. W. Gordon, B. Kendall, Molybdenum isotope evidence for mild environmental oxygenation before the Great Oxidation Event. *Geochim. Cosmochim. Acta* **74**, 6655–6668 (2010).
20. B. Kendall, G. A. Brennecka, S. Weyer, A. D. Anbar, Uranium isotope fractionation suggests oxidative uranium mobilization at 2.50 Ga. *Chem. Geol.* **362**, 105–114 (2013).
21. E. E. Stüeken, R. Buick, A. D. Anbar, Selenium isotopes support free $O_2$ in the latest Archean. *Geology* **43**, 259–262 (2015).
22. B. Kendall, R. A. Creaser, C. T. Reinhard, T. W. Lyons, A. D. Anbar, Transient episodes of mild environmental oxygenation and oxidative continental weathering during the late Archean. *Sci. Adv.* **1**, e1500777 (2015).
23. C. M. Ostrander, S. G. Nielsen, J. D. Owens, B. Kendall, G. W. Gordon, S. J. Romaniello, A. D. Anbar, Fully oxygenated water columns over continental shelves before the Great Oxidation Event. *Nat. Geosci.* **12**, 186–191 (2019).
24. J. Meixnerová, J. D. Blum, M. W. Johnson, E. E. Stüeken, M. A. Kipp, A. D. Anbar, R. Buick, Mercury abundance and isotopic composition indicate subaerial volcanism prior to the end-Archean "whiff" of oxygen. *Proc. Natl. Acad. Sci. U.S.A.* **118**, e2107511118 (2021).
25. T. S. Blake, M. E. Barley, Tectonic evolution of the Late Archaean to Early Proterozoic Mount Bruce Megasequence Set, Western Australia. *Tectonics* **11**, 1415–1425 (1992).
26. A. Pickard, SHRIMP U–Pb zircon ages of tuffaceous mudrocks in the Brockman Iron Formation of the Hamersley Range, Western Australia. *Aust. J. Earth Sci.* **49**, 491–507 (2002).
27. A. Trendall, W. Compston, D. Nelson, J. De Laeter, V. Bennett, SHRIMP zircon ages constraining the depositional chronology of the Hamersley Group, Western Australia. *Aust. J. Earth Sci.* **51**, 621–644 (2004).
28. B. Krapež, M. E. Barley, A. L. Pickard, Hydrothermal and resedimented origins of the precursor sediments to banded iron formation: Sedimentological evidence from the Early Palaeoproterozoic Brockman Supersequence of Western Australia. *Sedimentology* **50**, 979–1011 (2003).
29. D. M. Martin, P. Morris, Tectonic setting and regional implications of *ca* 2.2 Ga mafic magmatism in the southern Hamersley Province, Western Australia. *Aust. J. Earth Sci.* **57**, 911–931 (2010).
30. B. Rasmussen, I. R. Fletcher, S. Sheppard, Isotopic dating of the migration of a low-grade metamorphic front during orogenesis. *Geology* **33**, 773–776 (2005).
31. B. Rasmussen, J.-W. Zi, J. R. Muhling, D. J. Dunkley, W. W. Fischer, U-Pb dating of overpressure veins in late Archean shales reveals six episodes of Paleoproterozoic deformation and fluid flow in the Pilbara craton. *Geology* **48**, 961–965 (2020).
32. K. H. Williford, T. Ushikubo, K. Lepot, K. Kitajima, C. Hallmann, M. J. Spicuzza, R. Kozdon, J. L. Eigenbrode, R. E. Summons, J. W. Valley, Carbon and sulfur isotopic signatures of ancient life and environment at the microbial scale: Neoarchean shales and carbonates. *Geobiology* **14**, 105–128 (2016).
33. A. T. Greaney, R. L. Rudnick, R. T. Helz, R. M. Gaschnig, P. M. Piccoli, R. D. Ash, The behavior of chalcophile elements during magmatic differentiation as observed in Kilauea Iki lava lake, Hawaii. *Geochim. Cosmochim. Acta* **210**, 71–96 (2017).
34. G. R. Helz, T. P. Vorlicek, Precipitation of molybdenum from euxinic waters and the role of organic matter. *Chem. Geol.* **509**, 178–193 (2019).
35. L. Pitcher, R. T. Helz, R. J. Walker, P. Piccoli, Fractionation of the platinum-group elments and Re during crystallization of basalt in Kilauea Iki Lava Lake, Hawaii. *Chem. Geol.* **260**, 196–210 (2009).
36. H. E. Hartnett, R. G. Keil, J. I. Hedges, A. H. Devol, Influence of oxygen exposure time on organic carbon preservation in continental margin sediments. *Nature* **391**, 572–575 (1998).
37. S. D'Hondt, F. Inagaki, C. Alvarez Zarikian, H. Evans, N. Dubois, T. Engelhardt, T. Ferdelman, B. Gribsholt, R. N. Harris, B. W. Hoppie, J.-H. Hyun, J. Kallmeyer, J. Kim, J. E. Lynch, S. Mitsunobu, Y. Morono, R. W. Murray, B. K. Reese, T. Shimono, F. Shiraishi, D. C. Smith, C. E. Smith-Duque, A. J. Spivack, B. O. Steinsbu, Y. Suzuki, M. Szpak, L. Toffin, G. Uramoto, Y. Yamaguchi, Z. Guoliang, Z. Xiaohua, W. Ziebis, *Integrated Ocean Drilling Program Expedition 329 Preliminary Report; South Pacific Gyre Subseafloor Life; 9 October–13 December 2010* (IODP Management International, 2011).
38. M. E. Galvez, W. W. Fischer, S. L. Jaccard, T. I. Eglinton, Materials and pathways of the organic carbon cycle through time. *Nat. Geosci.* **13**, 535–546 (2020).
39. L. M. Ward, B. Rasmussen, W. W. Fischer, Primary productivity was limited by electron donors prior to the advent of oxygenic photosynthesis. *J. Geophys. Res. Biogeosci.* **124**, 211–226 (2019).
40. C. J. Bjerrum, D. E. Canfield, Ocean productivity before about 1.9 Gyr ago limited by phosphorus adsorption onto iron oxides. *Nature* **417**, 159–162 (2002).
41. P. Kharecha, J. Kasting, J. Siefert, A coupled atmosphere–ecosystem model of the early Archean earth. *Geobiology* **3**, 53–76 (2005).
42. W. W. Fischer, D. A. Fike, J. E. Johnson, T. D. Raub, Y. Guan, J. L. Kirschvink, J. M. Eiler, SQUID–SIMS is a useful approach to uncover primary signals in the Archean sulfur cycle. *Proc. Natl. Acad. Sci. U.S.A.* **111**, 5468–5473 (2014).

43. A. Pavlov, J. Kasting, Mass-independent fractionation of sulfur isotopes in Archean sediments: Strong evidence for an anoxic Archean atmosphere. *Astrobiology* **2**, 27–41 (2002).
44. B. P. Tissot, D. H. Welte, *Petroleum Formation and Occurrence* (Springer, 1984), pp. 160–198.
45. R. Littke, D. Baker, D. Leythaeuser, *Organic Geochemistry in Petroleum Exploration* (Elsevier, 1988), pp. 549–559.
46. P. R. Cobbold, A. Zanella, N. Rodrigues, H. Løseth, Bedding-parallel fibrous veins (beef and cone-in-cone): Worldwide occurrence and possible significance in terms of fluid overpressure, hydrocarbon generation and mineralization. *Mar. Pet. Geol.* **43**, 1–20 (2013).
47. M. G. Teixeira, F. Donzé, F. Renard, H. Panahi, E. Papachristos, L. Scholtès, Microfracturing during primary migration in shales. *Tectonophysics* **694**, 268–279 (2017).
48. R. E. Smith, J. Perdrix, T. Parks, Burial metamorphism in the Hamersley Basin, Western Australia. *J. Petrol.* **23**, 75–102 (1982).
49. R. White, R. Powell, T. Holland, T. Johnson, E. Green, New mineral activity–composition relations for thermodynamic calculations in metapelitic systems. *J. Metamorph. Geol.* **32**, 261–286 (2014).
50. A. S. Pepper, P. J. Corvi, Simple kinetic models of petroleum formation. Part I: Oil and gas generation from kerogen. *Mar. Pet. Geol.* **12**, 291–319 (1995).
51. F. Bourdelle, T. Parra, C. Chopin, O. Beyssac, A new chlorite geothermometer for diagenetic to low-grade metamorphic conditions. *Contrib. Mineral. Petrol.* **165**, 723–735 (2013).
52. R. J. Scott, S. Meffre, J. Woodhead, S. E. Gilbert, R. F. Berry, P. Emsbo, Development of framboidal pyrite during diagenesis, low-grade regional metamorphism, and hydrothermal alteration. *Econ. Geol.* **104**, 1143–1168 (2009).
53. R. A. Neely, S. R. Gislason, M. Ólafsson, A. J. McCoy-West, C. R. Pearce, K. W. Burton, Molybdenum isotope behaviour in groundwaters and terrestrial hydrothermal systems, Iceland. *Earth Planet. Sci. Lett.* **486**, 108–118 (2018).
54. D.-X. Kong, K. Cao, J.-F. Xu, J. Li, W. Li, Molybdenum isotope systematics of subduction-related magmas from the Zhongdian region: Assessing the mo fractionation behavior in magmatic-hydrothermal processes. *Ore Geol. Rev.* **133**, 104089 (2021).
55. M. Fakhraee, S. A. Crowe, S. Katsev, Sedimentary sulfur isotopes and Neoarchean ocean oxygenation. *Sci. Adv.* **4**, e1701835 (2018).
56. J. E. Johnson, S. M. Webb, K. Thomas, S. Ono, J. L. Kirschvink, W. W. Fischer, Manganese-oxidizing photosynthesis before the rise of cyanobacteria. *Proc. Natl. Acad. Sci. U.S.A.* **110**, 11238–11243 (2013).
57. D. L. Leach, D. Bradley, M. T. Lewchuk, D. T. Symons, G. de Marsily, J. Brannon, Mississippi valley-type lead–zinc deposits through geological time: Implications from recent age-dating research. *Mineral. Deposita* **36**, 711–740 (2001).
58. A. Bekker, B. Krapež, J. A. Karhu, K. Chamberlain, Reply to comment on "Bekker, A., Krapež, B., Karhu, J. A., 2020. Correlation of the stratigraphic cover of the Pilbara and Kaapvaal cratons recording the lead up to Paleoproterozoic icehouse and the GOE. Earth-Science Reviews, 211, 103,389" by Pascal Philippot, Bryan A. Killingsworth, Jean-Louis Paquette, Svetlana Tessalina, Pierre Cartigny, Stefan V. Lalonde**,** Christophe Thomazo, Janaina N. Ávila, Vincent Busigny. *Earth-Sci. Rev.* **218**, 103607 (2021).
59. D. Selby, R. A. Creaser, Re–Os geochronology of organic rich sediments: An evaluation of organic matter analysis methods. *Chem. Geol.* **200**, 225–240 (2003).
60. R. A. Creaser, P. Sannigrahi, T. Chacko, D. Selby, Further evaluation of the Re-Os geochronometer in organic-rich sedimentary rocks: A test of hydrocarbon maturation effects in the Exshaw Formation, Western Canada Sedimentary Basin. *Geochim. Cosmochim. Acta* **66**, 3441–3452 (2002).
61. J. L. Isbell, L. C. Henry, E. L. Gulbranson, C. O. Limarino, M. L. Fraiser, Z. J. Koch, P. L. Ciccioli, A. A. Dineen, Glacial paradoxes during the late Paleozoic ice age: Evaluating the equilibrium line altitude as a control on glaciation. *Gondwana Res.* **22**, 1–19 (2012).
62. R. J. Bain, Diagenetic, nonevaporative origin for gypsum. *Geology* **18**, 447–450 (1990).
63. X. Gu, P. J. Heaney, F. D. A. Reis, S. L. Brantley, Deep abiotic weathering of pyrite. *Science* **370**, eabb8092 (2020).
64. R. M. Gaschnig, R. L. Rudnick, W. F. McDonough, A. J. Kaufman, Z. Hu, S. Gao, Onset of oxidative weathering of continents recorded in the geochemistry of ancient glacial diamictites. *Earth Planet. Sci. Lett.* **408**, 87–99 (2014).
65. A. T. Greaney, R. L. Rudnick, S. J. Romaniello, A. C. Johnson, R. M. Gaschnig, A. D. Anbar, Molybdenum isotope fractionation in glacial diamictites tracks the onset of oxidative weathering of the continental crust. *Earth Planet. Sci. Lett.* **534**, 116083 (2020).
66. B. Rasmussen, R. Buick, Redox state of the Archean atmosphere: Evidence from detrital heavy minerals in ca. 3250–2750 Ma sandstones from the Pilbara Craton, Australia. *Geology* **27**, 115–118 (1999).
67. A. Hofmann, A. Bekker, O. Rouxel, D. Rumble, S. Master, Multiple sulphur and iron isotope composition of detrital pyrite in Archaean sedimentary rocks: A new tool for provenance analysis. *Earth Planet. Sci. Lett.* **286**, 436–445 (2009).
68. E. D. Swanner, A. Bekker, E. Pecoits, K. O. Konhauser, N. L. Cates, S. J. Mojzsis, Geochemistry of pyrite from diamictites of the Boolgeeda Iron Formation, Western Australia with implications for the GOE and Paleoproterozoic ice ages. *Chem. Geol.* **362**, 131–142 (2013).
69. A. P. Gumsley, K. R. Chamberlain, W. Bleeker, U. Söderlund, M. O. de Kock, E. R. Larsson, A. Bekker, Timing and tempo of the Great Oxidation Event. *Proc. Natl. Acad. Sci. U.S.A.* **114**, 1811–1816 (2017).
70. P. Philippot, J. N. Ávila, B. A. Killingsworth, S. Tessalina, F. Baton, T. Caquineau, E. Muller, E. Pecoits, P. Cartigny, S. V. Lalonde, T. R. Ireland, C. Thomazo, M. J. van Kranendonk, V. Busigny, Globally asynchronous sulphur isotope signals require re-definition of the Great Oxidation Event. *Nat. Commun.* **9**, 2245 (2018).
71. M. R. Warke, T. Di Rocco, A. L. Zerkle, A. Lepland, A. R. Prave, A. P. Martin, Y. Ueno, D. J. Condon, M. W. Claire, The Great Oxidation Event preceded a Paleoproterozoic "snowball Earth.". *Proc. Natl. Acad. Sci. U.S.A.* **117**, 13314–13320 (2020).
72. S. W. Poulton, A. Bekker, V. M. Cumming, A. L. Zerkle, D. E. Canfield, D. T. Johnston, A 200-million-year delay in permanent atmospheric oxygenation. *Nature* **592**, 232–236 (2021).
73. P. A. O'Day, N. Rivera Jr., R. Root, S. A. Carroll, X-ray absorption spectroscopic study of Fe reference compounds for the analysis of natural sediments. *Am. Mineral.* **89**, 572–585 (2004).
74. M. E. Fleet, XANES spectroscopy of sulfur in earth materials. *Can. Mineral.* **43**, 1811–1838 (2005).
75. L. Mayhew, S. Webb, A. Templeton, Microscale imaging and identification of Fe speciation and distribution during fluid-mineral reactions under highly reducing conditions. *Environ. Sci. Technol.* **45**, 4468–4474 (2011).
76. S. M. Webb, The microanalysis toolkit: X-ray fluorescence image processing software. *AIP Conf. Proc.* **1365**, 196–199 (2011).
77. S. M. Webb, SIXPack A graphical user interface for XAS analysis using IFEFFIT. *Phys. Scr.* **T115**, 1011–1014 (2005).
78. B. Rasmussen, I. R. Fletcher, Dating sedimentary rocks using in situ U-Pb geochronology of syneruptive zircon in ash-fall tuffs < 1 mm thick. *Geology* **38**, 299–302 (2010).
79. R. A. Stern, Y. Amelin, Assessment of errors in SIMS zircon U–Pb geochronology using a natural zircon standard and NIST SRM 610 glass. *Chem. Geol.* **197**, 111–142 (2003).
80. R. A. Stern, S. Bodorkos, S. L. Kamo, A. H. Hickman, F. Corfu, Measurement of SIMS instrumental mass fractionation of Pb isotopes during zircon dating. *Geostand. Geoanal. Res.* **33**, 145–168 (2009).
81. K. Ludwig, *Squid 2.50, A User's Manual* (Berkeley Geochronology Centre, 2009).
82. K. Ludwig, *User's Manual for Isoplot 3.75: A Geochronological Toolkit for Microsoft Excel* (Berkeley Geochronology Centre, 2012), vol. 5.
83. L. E. J. Ibach, Relationship between sedimentation rate and total organic carbon content in ancient marine sediments. *AAPG Bull.* **66**, 170–188 (1982).


**Acknowledgments:** We thank T. Present and Y. Guan for aid in SIMS data collection. We acknowledge the anonymous reviewers who gave critical and useful comments that greatly improved the manuscript. **Funding:** This research was supported by the Agouron Institute, NASA Exobiology, NSF-EAR 0739105 (T.D.R. and J.L.K.), the Packard Foundation, NSF Graduate Research Fellowships (S.P.S. and J.E.J.), and NASA Earth and Space Science Fellowship (S.P.S.). Portions of this research were carried out at the Stanford Synchrotron Radiation Lightsource, SLAC National Accelerator Laboratory, supported by the U.S. Department of Energy, Office of Science, Office of Basic Energy Sciences under contract no. DE-AC02-76SF00515. **Author contributions:** T.D.R., J.L.K., W.W.F., B.R., S.P.S., and J.E.J. designed research. T.D.R., W.W.F., and B.R. studied and sampled the rock cores. T.D.R., S.P.S., J.E.J., and W.W.F. performed secondary ion mass spectrometry analyses. S.P.S., J.E.J., and W.W.F. performed petrography and electron microscopy. S.P.S., J.E.J., S.M.W., and W.W.F. performed synchrotron-based spectroscopy. B.R. and J.-W.Z. developed geochronological data. S.P.S., J.E.J., W.W.F., B.R., and J.L.K. wrote the paper. **Competing interests:** The authors declare that they have no financial or other competing interests. **Data and materials availability:** All data needed to evaluate the conclusions in the paper are present in the paper and/or the Supplementary Materials.

Submitted 27 May 2021
Accepted 17 November 2021
Published 5 January 2022
10.1126/sciadv.abj7190

ScienceAdvances

# Reexamination of 2.5-Ga “whiff” of oxygen interval points to anoxic ocean before GOE

Sarah P. SlotznickJena E. JohnsonBirger RasmussenTimothy D. RaubSamuel M. WebbJian-Wei ZiJoseph L. KirschvinkWoodward W. Fischer

*Sci. Adv.*, 8 (1), eabj7190. • DOI: 10.1126/sciadv.abj7190